Transition between solid and liquid state of yield-stress fluids under purely extensional deformations

Stylianos Varchanis[a], Simon J. Haward[b], Cameron C. Hopkins[b], Alexandros Syrakos[a,1], Amy Q. Shen[b], Yannis Dimakopoulos[a], and John Tsamopoulos[a,2]

[a]Laboratory of Fluid Mechanics and Rheology, Department of Chemical Engineering, University of Patras, 26500 Patras, Greece; and [b]Micro/Bio/Nanofluidics Unit, Okinawa Institute of Science and Technology Graduate University, Okinawa 904-0495, Japan

Edited by David A. Weitz, Harvard University, Cambridge, MA, and approved April 16, 2020 (received for review December 18, 2019)

We report experimental microfluidic measurements and theoretical modeling of elastoviscoplastic materials under steady, planar elongation. Employing a theory that allows the solid state to deform, we predict the yielding and flow dynamics of such complex materials in pure extensional flows. We find a significant deviation of the ratio of the elongational to the shear yield stress from the standard value predicted by ideal viscoplastic theory, which is attributed to the normal stresses that develop in the solid state prior to yielding. Our results show that the yield strain of the material governs the transition dynamics from the solid state to the liquid state. Finally, given the difficulties of quantifying the stress field in such materials under elongational flow conditions, we identify a simple scaling law that enables the determination of the elongational yield stress from experimentally measured velocity fields.

elastoviscoplastic materials | yield stress | yield strain | viscoplastic materials | extensional flow

The term elastoviscoplastic (EVP) refers to a very wide class of fluids that behave either as solids or as liquids when exposed to different stress conditions. More specifically, when the material is exposed to a stress that is below a critical value, namely the yield stress (τ_y), it behaves like an elastic solid; otherwise, it flows like a complex fluid. This behavior stems from the self-interaction (jamming, glass transition, attractive forces) of the internal microstructure of the material (1, 2). The most common examples of EVP fluids stem from colloids, dense suspensions, emulsions, foams, and gels (3), whose microstructure features a mesoscopic length scale of the order of 10 μm. Recent studies have generalized the application of elastoviscoplasticity to materials with a larger length scale in their internal structure, such as lava flow (4) and the description of the relaxation process of impact crater topography on planetary satellites (5).

Despite the wide diversity of applications EVP materials are involved in, very little is known regarding the normal stresses such materials develop. On the contrary, the characterization of EVP fluids is based on shear rheology and the value of yield stress is measured only in shear flows. This is because the normal stresses that develop in EVP materials are very difficult to measure due to, e.g., nonhomogeneity of the flow field, residual stresses, and of course, instrument sensitivity. In addition, producing a shear-free flow field is a great challenge. Very recently, Zhang et al. (6) performed filament stretching experiments of EVP materials on slippery surfaces and achieved a reasonable approximation of uniaxial elongational flow. They found the ratio of the yield stress measured in uniaxial elongation to its value measured in shear flow to be greater, by a factor of 1.5, than the value predicted by the ideal viscoplastic theory. Moreover, de Cagny et al. (7) combined steady and oscillatory measurements of normal stresses in shear flows of EVP materials. They found that the first normal stress difference developed in shear flow is positive, that the second normal stress difference is negative, and that both are comparable in magnitude to the shear stress. They also identified a yield normal stress, something that again cannot be predicted by the ideal viscoplastic theory. Numerous other observations, such as the loss of fore-aft symmetry and the presence of a "negative wake" in the flow field during the sedimentation of a single particle in a Carbopol gel (8, 9), or cusped bubble shapes rising in a Carbopol gel (10, 11), have emphasized the importance of studying the underlying physics in the development of normal stresses in yield stress materials (12). Although thixotropy, viz. the dependence of the material parameters (yield stress, viscosity, etc.) on the deformation history, could induce similar effects (13), in this study we will focus only on the normal stresses that develop in simple (nonthixotropic) yield-stress fluids, whose material properties are constant and do not depend on the deformation history.

Results and Discussion

To overcome the aforementioned difficulties and get an insight in the elongational and yielding properties of EVP materials, we study their flow in the optimized shape cross-slot extensional rheometer (OSCER) (*SI Appendix*, Fig. S1 and refs. 14 and 15) (Fig. 1 *A* and *B*). The OSCER is based upon the usual planar cross-slot geometry, with incoming flow through the two opposite

Significance

The stress-induced transition from solid to liquid state is commonly referred to as "yielding." Yield-stress materials, including pastes, muds, blood, crude oil, and condiments like mayonnaise, have solid-like properties at rest but can be made to yield and flow under sufficient applied stress. Despite their ubiquity and importance, the existing 100-y-old theory describing the behavior of such materials is only well verified under basic conditions of applied shear stress and assumes that the solid state is undeformable. Experiments and simulations conducted under pure extension provide fundamental information on the behavior of yield-stress materials and demand an overhaul of the current standard theory in order to account for material deformation in the solid-like state prior to yielding and flow.

Author contributions: S.V., S.J.H., C.C.H., and J.T. designed research; S.V., S.J.H., C.C.H., A.S., A.Q.S., Y.D., and J.T. performed research; S.J.H., A.Q.S., Y.D. and J.T. provided experimental tools; S.V., S.J.H., and A.S. analyzed data; Y.D. and J.T. provided computational power, and S.V., S.J.H., C.C.H., A.S., A.Q.S., Y.D., and J.T. wrote the paper.

The authors declare no competing interest.

This article is a PNAS Direct Submission.

[1]Present address: Department of Mechanical and Manufacturing Engineering, University of Cyprus, 1678 Nicosia, Cyprus.

[2]To whom correspondence may be addressed. Email: tsamo@chemeng.upatras.gr.

This article contains supporting information online at https://www.pnas.org/lookup/suppl/doi:10.1073/pnas.1922242117/-/DCSupplemental.

First published May 20, 2020.

vertical channels and flow out through the two opposite horizontal channels, as presented in Fig. 1*B*. Assuming symmetry of the flow field, this configuration results in a free stagnation point at the center of the OSCER device, where we locate the coordinate origin. The OSCER geometry has been numerically optimized for Newtonian fluids (14) in order to provide a shear-free, extensional flow field in a finite region around the stagnation point. Near the walls, shearing effects minimize the stretching of fluid elements, but the nearly stagnant fluid in the salient corners of the device helps "self-lubricate" the flow. Moreover, the device generates a very good approximation of two-dimensional flow field due to its large depth, $D = 2.1$ mm and high aspect ratio $\alpha = D/H = 10.5$ (see *SI Appendix*, Fig. S1 for a three-dimensional sketch of the OSCER), where $H = 200$ μm is the width of the channels (Fig. 1*B*). Streamlines near the center of the OSCER closely approximate hyperbolae in Newtonian fluids, with a singular hyperbolic point occurring in the geometric center of the device (the flow stagnation point). Here, the flow velocity is zero, but the strain rate is still finite, and the long residence time of fluid elements in this locality results in the accumulation of very high fluid strains, eventually leading to steady planar elongation. The EVP fluid that we have used in the experiments is a 20% aqueous solution of Pluronic F127 (Fig. 1 *C*–*E*). The Pluronic solution has the property of being a Newtonian liquid at low temperature ($T <$ 22 °C), but is a gel at higher temperature (16), and in its gel state it is well described by constitutive equations for simple yield-stress fluids (17). Moreover, when the Pluronic solution is found in its gel state, at temperatures greater than but not too far away from its gelation temperature, it does not exhibit thixotropic effects; see Fig. 1*C* (*SI Appendix* and ref. 17).

The EVP flow in the OSCER is simulated (18) using one of the simplest constitutive equations proposed by Saramito (19) that can predict all of the basic rheological properties of such a material. These are 1) elastic solid behavior in the solidified state, 2) weak viscoelastic fluid behavior in the liquid state and, 3) strain-rate thinning effects at high deformation rates. The equation that describes the evolution of the stresses is as follows:

$$\underbrace{\frac{1}{G}\overset{\nabla}{\boldsymbol{\tau}}}_{\substack{\text{Elastic}\\ \text{deformation}\\ \text{rate}}} + \underbrace{\max\left(0, \frac{\tau_d - \tau_y}{K\tau_d^n}\right)^{1/n}\boldsymbol{\tau}}_{\text{Viscoplastic deformation rate}} = \underbrace{\dot{\boldsymbol{\gamma}}}_{\substack{\text{Total}\\ \text{deformation}\\ \text{rate}}}. \qquad [1]$$

In this so-called Saramito–Herschel–Bulkley (SRM/HB) model, G is the elastic modulus, K is the consistency index, and n is the Herschel–Bulkley exponent that governs the strain-rate thinning of the material. The symbol ∇ over the stress tensor $\boldsymbol{\tau}$ denotes the upper convected derivative; τ_d, the magnitude of the deviatoric part of $\boldsymbol{\tau}$; and $\dot{\boldsymbol{\gamma}}$, the deformation rate tensor. Note that for $G \to \infty$, the elastic term vanishes, and the model reduces to the ideal viscoplastic Herschel–Bulkley model. Additionally, we define the yield strain of the material $\varepsilon_y = \tau_y/G$ and the plastic number $Pl = \tau_y/(\tau_y + K(0.214U/H)^n)$, where U is the mean velocity in each channel of the OSCER, far away from the stagnation point (Fig. 1*B*). The quantity $0.214U/H$ represents the apparent extension rate ($\dot{\varepsilon}$) at the stagnation point (15). The yield strain ε_y is introduced as a dimensionless number that expresses an estimation of the maximum deformation (not necessarily shear) that the solid can sustain prior to yielding and should not be confused with the shear yield strain that is monitored by Dinkgreve et al. (20). The plastic number varies in the range $0 < Pl < 1$, where $Pl \to 1$ implies elastic-solid–like response, and $Pl \to 0$ implies fluid-like response. The plastic number is related to the Bingham number via the relation: $Bn = Pl/(1 - Pl)$. Due to the small scale of the OSCER device, inertia is found to be negligible for all flow rates examined, and thus, the EVP flow is governed by only three parameters: ε_y, Pl, and n. The parameters of the constitutive equation are estimated by performing nonlinear regression to rheometric shear data. More specifically, the elastic modulus ($G = 8{,}500$ Pa) is extracted from oscillatory shear data, while the rest of the properties ($K = 30$ Pa·s^n, $\tau_y = 133$ Pa and $n = 0.31$) are estimated by performing nonlinear regression to the flow curve (Fig. 1 *C*–*E*). Thus, the yield strain of the Pluronic solution is found to be $\varepsilon_y = 0.016$. As shown by Varchanis et al. (21) and can be seen in Fig. 1 *D* and *E*, the SRM/HB model predicts a linear elastic solid response in the linear regime ($\gamma_0 \to 0$), something that does not hold for the Pluronic solution. This could be due to a viscous or

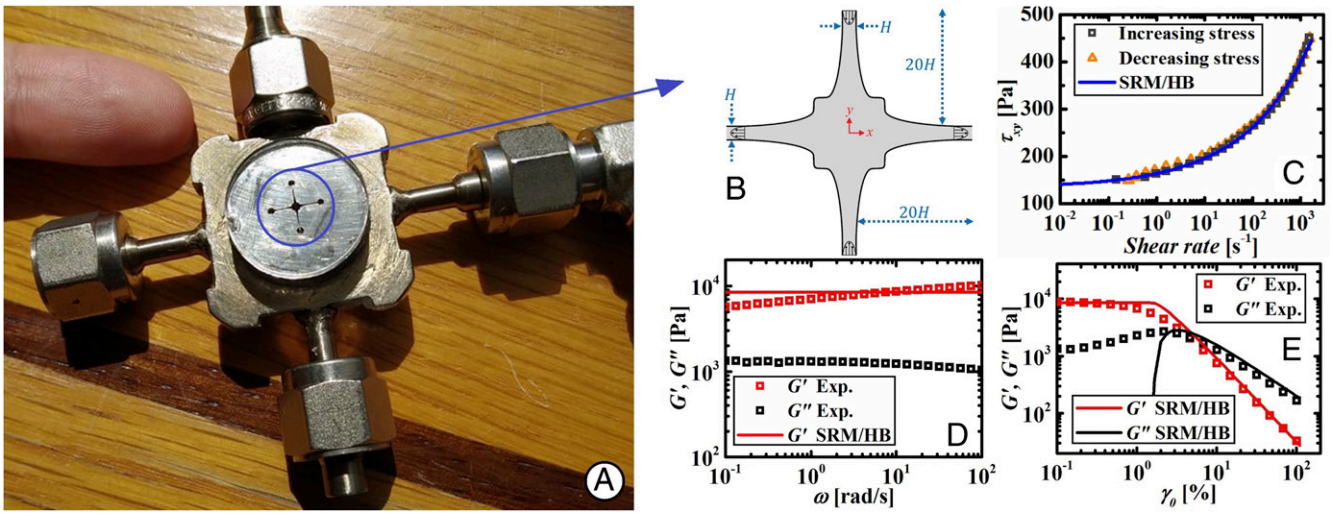

Fig. 1. (*A*) OSCER near the index finger of an adult. The extensional flow evolves in the region inside the blue circle. (*B*) Schematic of the OSCER around the stagnation point. (*C*) Steady-state flow curve obtained by increasing and decreasing stress ramps. (*D*) Small-amplitude oscillatory shear (SAOS) and (*E*) large-amplitude oscillatory shear (LAOS) data of the Pluronic solution. Symbols denote experimental measurements; lines denote the predictions of the Saramito–Herschel–Bulkley (SRM/HB) model.

plastic (22) component in the solid state, or to other mechanisms like kinematic hardening (9, 23). However, when considering flows with spatial variations, and especially flows that reach a steady state, the deformations that the material undergoes are necessarily nonlinear. So, in such simulations and comparisons with experiments, we believe that it is more crucial to capture the material's response in the nonlinear regime, which the SRM/HB model performs well (Fig. 1*E*).

Proceeding to the flow in the OSCER, in Fig. 2 we present comparisons between the experimental and theoretical steady-state flow profiles for $Pl = 0.88$ and $Pl = 0.52$. The experimental velocity profiles are obtained using microparticle image velocimetry (μ-PIV) (see *Materials and Methods* for details). The approximately hyperbolic shape of the streamlines reveals that we can achieve steady planar elongation (*SI Appendix*, Figs. S6–S9) of an EVP material in the OSCER. Initially, we consider the flow of Pluronic in the OSCER for a low extension rate $\dot{\varepsilon} = 0.22\ s^{-1}$, resulting in $Pl = 0.88$. Since Pl is close to 1, the flow will be dominated by plasticity and the material will feature an elastic-solid–like behavior, although it is in a liquid state (plastic deformation regime) around the stagnation point (Fig. 2*A*). This means that the flow will reach a steady state under a low deformation rate, which will cause the stresses to be slightly above the yield stress. Note that part of the stress that it carries is elastic, and thus, part of the deformation (proportional to ε_y) that it is exposed to is recoverable. This type of flow regime can be called "elastoplastic." Furthermore, by comparing the magnitude of the velocity contours and the streamlines at the left-hand (numerical) and right-hand (experimental) sides of Fig. 2*A*, it is clear that the simulation can capture the experiment with good quantitative accuracy. Observing the unyielded surfaces, which are predicted from the simulations using the von Mises criterion and are depicted with blue color in Fig. 2*B*, we see that there is trapped material that remains unyielded in the salient corners of the OSCER. In addition, we locate four large unyielded regions around the stagnation point with curved streamlines passing through them. This is quite strange, as one would expect that these curved streamlines would imply deformation at these areas. The presence of these unyielded regions is explained physically by the fact that they undergo solid body rotation. It is well known that the unyielded part of a yield-stress material undergoes a simple translation in Poiseuille flow and is surrounded by yielded material (24). Here, we find that the unyielded part of such a material can undergo the only other basic type of motion a solid can undergo, i.e., solid body rotation. As shown in Fig. 2*C*, the streamlines inside the unyielded "plug" regions form concentric circular arcs, centered at the points (±0.55 mm, ±0.55 mm). These four points are the centers of solid body rotation of the four plug regions, respectively. Furthermore, we drew circles from this center with different radii (R_i) to demonstrate that the streamlines coincide with these circles inside the unyielded region only. Note that the distance between the streamlines in Fig. 2*C* varies outside the unyielded region but remains constant inside. Hence, the material solidifies upon entry into the unyielded region, rotates as a solid body, and reliquefies upon exiting that region.

These transitions of the material can be further understood by Fig. 2*D*, which shows the trajectories of two (magnified) point particles, one in yellow and the other in green color. Of course, the flow is steady in the Eulerian frame, but unsteady in the Lagrangian (particle) frame. The two particles enter this quadrant of the flow domain from the inflow above, follow two different streamlines, and exit at the outflow in the right. We also denote their distance with a gray line. Because of the flow configuration, the left streamline corresponds to a higher velocity. For this reason, the green particle in the streamline with the larger curvature is chosen to be ahead of the yellow particle, when they are initially identified at the same instant t_1. The two particles initially are in the liquid region, which undergoes local deformation, and so their distance decreases according to the local flow field. However, when they enter the unyielded region, they can only undergo a solid body rotation and their distance remains nearly constant, because the material here has no visible deformation. Thus, the particles remain on the same radius, as clearly seen at the time instants t_2 and t_3. This solid body rotation is characterized by a linear velocity ωR_i, where ω is the angular velocity and R_i is the distance from the center of rotation. When the particles exit the unyielded region, the surrounding material can again deform and so their distance changes, as clearly seen at instant t_4. As in Poiseuille flow, the unyielded region remains stationary in the Eulerian frame, but in fact it is composed of different fluid elements at each time instant. However, in the OSCER geometry, this region has a finite extent and is surrounded by flowing material. This makes it necessary for material to enter and exit this region in the Lagrangian frame. A related movie is provided (Movie S1).

Increasing the extension rate by an order of magnitude at a time, we eventually reach $\dot{\varepsilon} = 90\ s^{-1}$ ($Pl = 0.52$) and observe the same good agreement between theoretical predictions and experiments even for such high extension rates (Fig. 2*E*). Moreover, the flow pattern remains similar to the previous one at lower extension rate (Fig. 2*A*), with the difference that the unyielded regions have shrunk significantly (Fig. 2*F*) due to the excess stress induced by the elongation of the Pluronic solution.

Next, in Fig. 3 *A*–*C*, we present a direct quantitative comparison between the predicted and experimental values of the x-component of velocity at the symmetry plane $y = 0$, for values of $\dot{\varepsilon}$ increasing by an order of magnitude at a time from 0.22 to 22 s^{-1}. The match is very good for all values of $\dot{\varepsilon}$. In the four cases presented in Figs. 2 and 3, the maximum relative error $[(u_{exp} - u_{SRM/HB})/u_{exp}]$ in the velocity field is about 19%, and it is located close to the outflow channel of the OSCER. Around the stagnation point ($-0.5 < x < 0.5$ mm), the relative error is less than 5% in all cases. In particular, for $Pl = 0.77$ and $Pl = 0.62$, the relative error between theory and experiment is less than 5% over the entire range of x (Fig. 3 *B* and *C*). Given the good agreement between theory and experiment achieved in this and a previous study (9), it is evident that the simplification of modeling the solid state as a linear elastic solid is successful and that the SRM/HB model can accurately describe nonlinear flows of simple yield-stress fluids.

Contrary to the velocity profiles obtained with Newtonian fluids (Fig. 3, dotted lines) and viscoelastic polymer solutions (15), the plots obtained with the EVP fluid are not straight lines, and therefore the velocity derivative along this axis is not constant. Instead, the experimental velocity distribution exhibits "bumps," which are captured precisely by the simulation. These bumps are caused by the presence of the unyielded regions and the component of solid body rotation that they introduce to the flow, which disturbs the expected hyperbolic flow field. As the fluid particles pass between the unyielded regions, they accelerate and subsequently decelerate, causing this breakage in the u_x velocity distribution along the $y = 0$ plane. However, apart from the fact that these bumps disturb the homogeneity of the extensional flow field around the stagnation point, the flow is still shear-free in a large region around the stagnation point (*SI Appendix*, Figs. S8 and S9). Such bumps in the outlet velocity profile can be considered as a fingerprint of the plasticity of the fluid.

In an effort to quantify the extensional stress in our experimental setup, we perform excess pressure drop measurements. The pressure drop ΔP is measured across an inlet and an outlet of the device as a function of the imposed extensional rate. Two measurements of ΔP are made. Firstly, ΔP_{total} is measured with

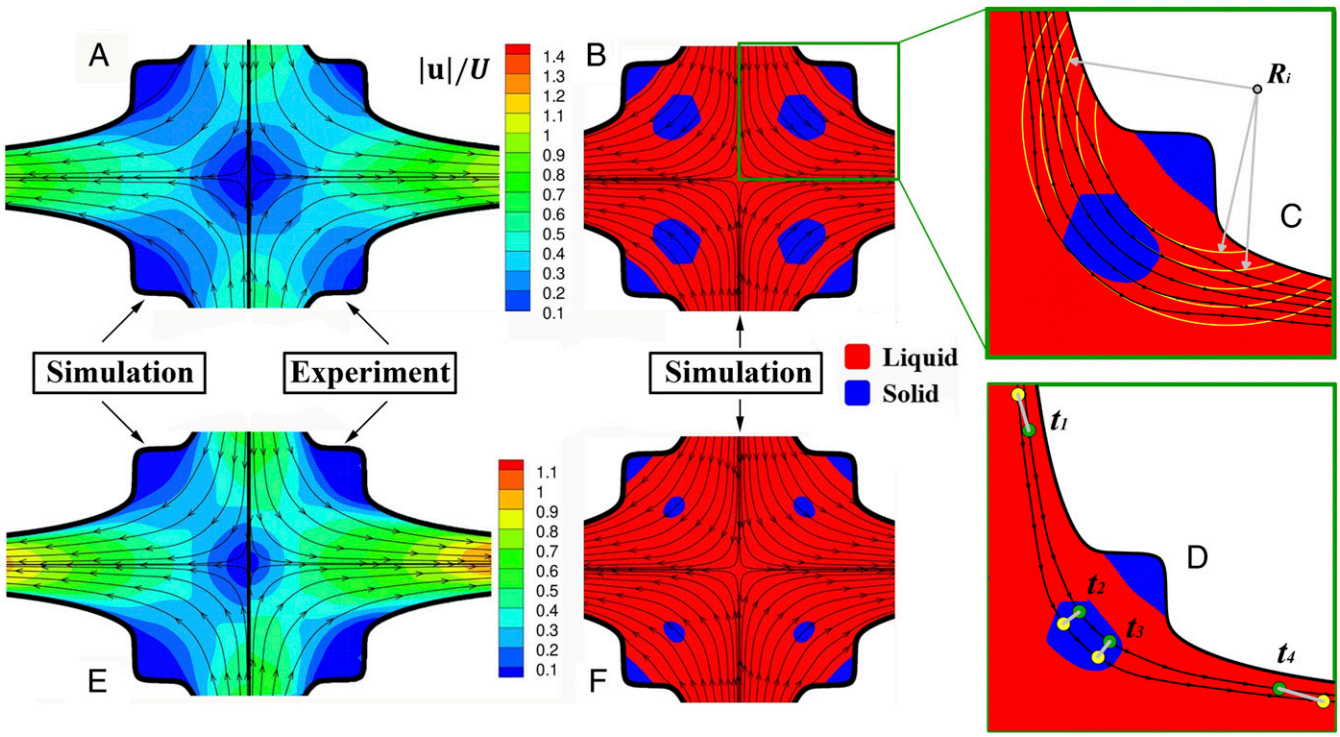

Fig. 2. (*A*) Steady-state predictions of the simulation (*Left* half) and experimental μ-PIV measurements (*Right* half) for the magnitude of velocity at $\dot{\varepsilon} = 0.22\ s^{-1}$ ($PI = 0.88$). The contours are set to the same values for both the simulation and the experiment making the comparison quantitative. (*B*) Streamlines of the flow, superimposed to the yield surfaces at $\dot{\varepsilon} = 0.22\ s^{-1}$ ($PI = 0.88$). The yield surfaces are predicted using the von Mises criterion from the stress field obtained by the simulations. (*C*) Solid body rotation of the unyielded regions in the OSCER in a close-up of the *Upper Right* part of *B*. (*D*) Trajectories of particles released at the same instant t_1 located in the unyielded region at times t_2 and t_3. (*E* and *F*) Same as *A* and *B* but for a much stronger extension rate $\dot{\varepsilon} = 90\ s^{-1}$ ($PI = 0.52$).

all of the channels of the OSCER open and therefore under planar elongational flow with a stagnation point. Second, the shear stress is quantified by measuring ΔP_{shear} with only one pair of inlet/outlet channels open (see *Materials and Methods* and *SI Appendix* for details). ΔP_{shear} is expected to be smaller than ΔP_{total} because of the elimination of the extensional region and, hence, the lack of the increase in the viscosity there (proportional to the Trouton ratio). Thus, a first-order approximation of the extensional stresses at the stagnation point can be obtained by the relation: $\tau_{xx} - \tau_{yy} \approx \Delta P_{\text{ext}} = \Delta P_{\text{total}} - \Delta P_{\text{shear}}$ (*SI Appendix* and refs. 15 and 25). The results are plotted in Fig. 4*A*, where the data points are the average of three measurements and error bars represent 1 standard deviation. The error bars are clearly very large, which is a result of the fact that the microstructure of Pluronic consists of somewhat inextensible blob-like polymer micelles inducing small elastic effects and a small Trouton ratio, hence the very small difference ΔP_{ext} relative to the large values of ΔP_{total} and ΔP_{shear}. However, over most of the $\dot{\varepsilon}$ range, the data points are of similar magnitude and trend to the prediction of our model simulations, also shown on Fig. 4*A*. Fig. 4*A* demonstrates that as the extension rate tends to zero, $\tau_{xx} - \tau_{yy}$ does not tend to zero but to a finite value. This plateau resembles the plateau observed in simple shear flow experiments and defines the normal yield stress in planar elongation ($\sigma_{y,e}$). The ideal viscoplastic theory (*SI Appendix*) predicts that $\sigma_{y,e} = 2\ \sigma_{y,s}$, where $\sigma_{y,s}$ is the value of the shear stress plateau in simple shear experiments. For the case of Pluronic, we find that the ratio $\sigma_{y,e}/\sigma_{y,s}$ equals 2.04, which is in good agreement with the ideal viscoplastic theory, especially since the flow in the OSCER exhibits a small deviation from ideal planar elongation due to the

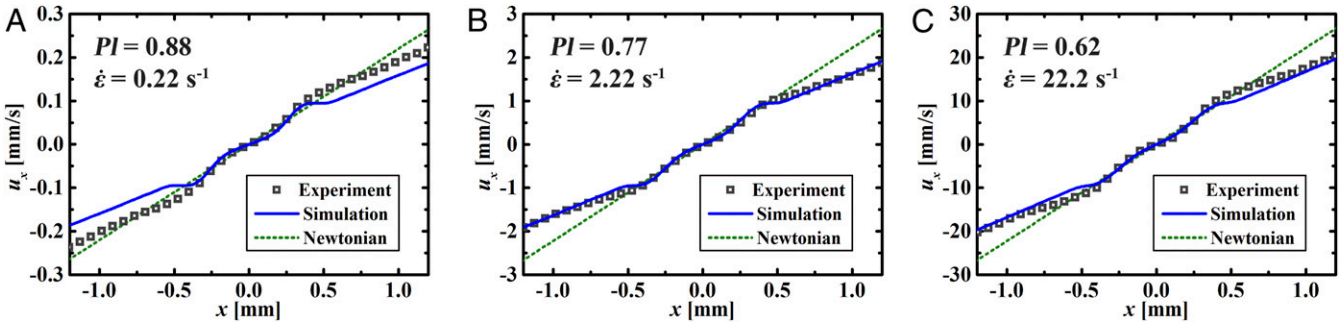

Fig. 3. (*A–C*) *x*-component of velocity as predicted by simulation versus experimental μ-PIV measurements at the midplane $y = 0$ for different extension rates. The theoretical and experimental curves for Newtonian liquids fall on top of each other.

unyielded plugs. For simplicity, we will refer to the quantity $\sigma_{y,e}/\sigma_{y,s}$ as the "yield-stress Trouton ratio" (Tr_y).

Since previous studies have reported that the value of Tr_y can deviate from the value that ideal viscoplastic theory predicts (6, 26, 27), we perform a parametric analysis to investigate whether we can reach a similar conclusion for a material with different rheological properties. Since we are interested in the response of EVP materials close to yielding conditions, strain-rate thinning effects are not expected to be important; consequently, we will examine the effect of yield strain on the flow patterns. It is noteworthy that increasing the yield strain leads to a more elastic solid state. Thus, the material can sustain more deformation prior to yielding. As is clear in Fig. 4*A*, the yield strain has almost no effect on the value of $\tau_{xx} - \tau_{yy}$ at the stagnation point as $\dot{\varepsilon} \to 0$, and all four theoretical curves for different values of ε_y collapse. The value of $\tau_{xx} - \tau_{yy}$ at the stagnation point is not affected by ε_y at the limit of $Pl \to 1$, simply because the material is always found in a liquid state at the stagnation point with its network destructed. It can also be shown analytically that in ideal planar extension, $\sigma_{y,e}$ does not depend on ε_y (*SI Appendix*). Apparently, for materials that feature strong elasticity, viscoelastic effects will arise at high extension rates; this is the case for $\varepsilon_y = 0.5$. Despite the negligible difference in the value of $\tau_{xx} - \tau_{yy}$ as $\dot{\varepsilon} \to 0$, observing Fig. 4 *B*–*E*, we realize that ε_y has a dramatic effect on the flow field around the stagnation point for values greater than 0.2. The unyielded regions are pushed toward the outflow, the center of rotation changes position, and as ε_y increases further, we can also observe that the solid body motion becomes more complex, since in addition to rotation, the solid region also deforms elastically. Examining the streamlines in the unyielded region in Fig. 4*E* ($\varepsilon_y = 0.5$), we observe that they are not perfect circles anymore. Also new unyielded regions arise and the spatial distribution of $\tau_{xx} - \tau_{yy}$ is no longer symmetric with respect to the $y = x$ line. All these are clear signs of elasticity. Nevertheless, we find that in the homogeneous elongation region, ε_y does not affect the value of $\tau_{xx} - \tau_{yy}$; thus, it does not affect Tr_y. Consequently, based on our results, the deviation of Tr_y from 2 is not related to the elongational yielding dynamics of EVP materials.

Thus, we turn our attention to the denominator of Tr_y, the value of yield stress in shear flow. Assuming ideal shear and planar elongational conditions, we plot in Fig. 5*A* Tr_y versus ε_y for different values of n. In fact, it is clear in Fig. 5*A* that Tr_y is only a function of the yield strain. For low values of ε_y, the EVP theory reduces to the old ideal viscoplastic theory and Tr_y is equal to 2. On the contrary, for yield strains higher than 0.2, this ratio increases considerably, reaching up to 2.6 for $\varepsilon_y = 1$. As mentioned above, this effect has been observed experimentally, but no physical explanation was offered. Based only on the fact that the material is allowed to attain deformation prior to yielding (*SI Appendix*), we give the following physical interpretation: As ε_y increases, the solid state becomes more elastic; thus, normal stresses in it increase. This means that normal stresses start to contribute to the von Mises criterion appreciably. So, in simple shear, the τ_{xy} contribution to the von Mises criterion decreases. Consequently, yielding can be achieved at a lower value of τ_{xy}. Thus, the denominator decreases and Tr_y increases.

Finally, since a direct measurement of $\sigma_{y,e}$ in elongation is not feasible (as is clear from the experimental error bars in Fig. 4*A*, the excess pressure drop cannot reliably quantify $\tau_{xx} - \tau_{yy}$), we seek an alternative method to estimate $\sigma_{y,e}$ from the flow field measured in the OSCER. Based on the characteristic asymmetry that is caused by the increase of ε_y in the flow field (Fig. 4 *B*–*E*), we define a local flow asymmetry parameter:

$$LA = \frac{|u_x|_{(x=0.5\ \mathrm{mm}, y=0)} - |u_y|_{(x=0, y=0.5\ \mathrm{mm})}}{|u_x|_{(x=0.5\ \mathrm{mm}, y=0)} + |u_y|_{(x=0, y=0.5\ \mathrm{mm})}}, \qquad [2]$$

which compares the absolute value of the x-component of velocity at the position ($x = 0.5$ mm, $y = 0$) to the absolute value of the y-component of velocity at ($x = 0$, $y = 0.5$ mm). In fact, this parameter can quantify elastic effects in the OSCER and is easily computed from the μ-PIV measurements. When LA equals 0, the flow is Newtonian-like and approximates ideal planar extension. When it deviates from 0, then elastic effects are present, and the flow becomes asymmetric with respect to the $y = x$ line. As Fig. 5*B* clearly shows, when Pl tends to 1 (viz. plastic effects dominate the flow), LA features a universal dependence on ε_y.

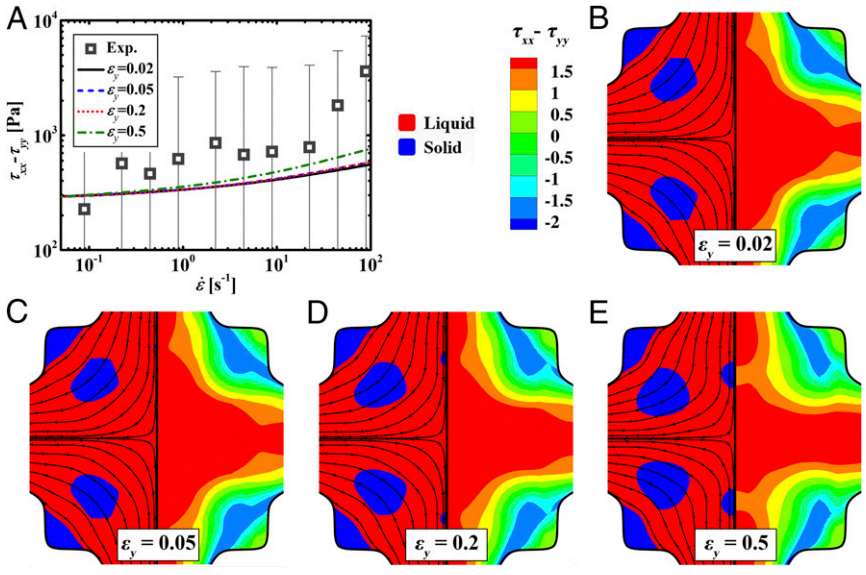

Fig. 4. (*A*) Normal stress difference $\tau_{xx} - \tau_{yy}$ estimated from excess pressure drop experiments (square symbols) and from simulations at the stagnation point (lines) versus apparent extension rate for four values of the yield strain. (*B*–*E*) Simulation results for the streamlines of the flow, superimposed to the yield surfaces (*Left*) and contours of $(\tau_{xx} - \tau_{yy})/(\tau_y + K\dot{\varepsilon}^n)$ (*Right*) at $\dot{\varepsilon} = 0.22\ s^{-1}$ ($Pl = 0.88$) for the same four values of the yield strain.

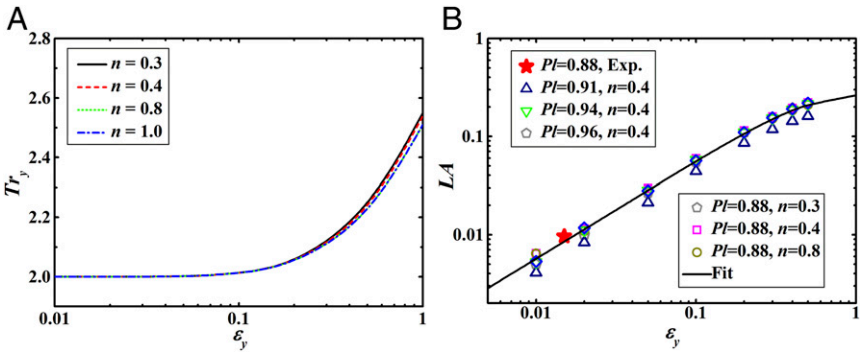

Fig. 5. (*A*) Yield-stress Trouton ratio versus yield strain for various values of the strain rate thinning parameter. (*B*) Local asymmetry parameter versus yield strain for various flow conditions.

This relation is well described by the following: $LA = 0.27\tanh(2.1\varepsilon_y)$. Thus, by measuring LA with μ-PIV and by measuring G in oscillatory shear, we can obtain $\sigma_{y,e}$ from the OSCER flow under steady state elongational conditions.

Summarizing, we have managed to experimentally subject a simple (nonthixotropic) yield-stress material to steady, pure planar elongational flow conditions. The flow patterns indicate that the yield strain of the material governs the transition dynamics from the solid state to the liquid state. Using a simple theory that allows the solid state to deform prior to yielding, we have shown that the ratio of the elongational to the shear yield stress can deviate from the standard value that the ideal visco-plastic theory predicts. In fact, this yield-stress Trouton ratio (Tr_y) depends only on the yield strain (ε_y) of the material, which is not considered in the ideal theory. Despite the fact that current rheometric methods cannot quantify the stress field in an EVP fluid, we have identified a universal scaling of the OSCER flow asymmetry with ε_y that can lead to the estimation of the elongational yield stress. Nevertheless, it is crucial to note that measuring $\sigma_{y,e}$ is important only when ε_y exceeds a value of 0.2. For $\varepsilon_y < 0.2$, as we show above, Tr_y will attain values equal to 2, so a measurement of the yield stress in shear flow is adequate to describe the yielding dynamics of the material.

Materials and Methods

Rheological Characterization. Rheometric shear tests were performed with an Anton Paar MCR 502 rheometer at room temperature (24 °C). A 50-mm-diameter cone-and-plate geometry (1° cone angle) with roughened surfaces (to avoid any wall slip) was used. To obtain the flow curve, and ensure that no thixotropic effects are present in the Pluronic solution, we used three different protocols regarding shear measurements:

1) In the first protocol, the sample was presheared at 0.01 s^{-1} for 5 min before immediately starting the stress sweep. No time limit was imposed at each applied stress. Through internal steady-state sensing, the rheometer determined when the measurement had reached steady state before moving to the next stress level. The stress was first increased in steps and immediately afterward decreased. The experimental data, along with the SRM/HB predictions, are presented Fig. 1*C*.
2) In the second protocol, we performed stress-controlled ramps with various waiting times between each stress increase/decrease. The waiting times that we used are 20, 10, 5, and 1 s. These results are presented in *SI Appendix*. All of the data coincide, and there is clearly no hysteresis over these stress values and waiting times.
3) Finally, we performed the protocol proposed by Dinkgreve et al. (13). In this test, the sample was presheared for 30 s at a shear rate equal to 100 s^{-1}, followed by a 30-s rest, and then increasing/decreasing shear-rate ramps from 0.01 to 500 s^{-1}, with 10-s waiting time. Again, these results are presented in *SI Appendix*, and no thixotropic effects are visible.

Prior to the amplitude sweep, the sample was presheared at 0.01 s^{-1} for 5 min. The sample was then allowed to rest for 1 min before beginning the oscillatory measurement. The angular frequency was fixed at 1 rad/s, and the strain amplitude was increased logarithmically from 0.01 to 100%. From the amplitude sweep, a suitable strain amplitude within the linear viscoelastic regime was selected (0.1 or 0.2%). That strain amplitude was then used for a frequency sweep on the same sample without replacing it. The angular frequency was decreased logarithmically from 100 to 0.1 rad/s.

Fluid Loading and Flow Control in the OSCER Device. The 20 wt% Pluronic solution used as a model EVP fluid in the planar elongational flow experiments in the OSCER device has the convenient property of a critical gelation temperature (16). Below around 22 °C, the fluid behaves as a relatively low viscosity Newtonian fluid. This allows the fluid to be loaded into the OSCER device and the connecting tubing and syringes at low temperature in a cold storage room, and for any trapped air bubbles to be evacuated from the system. Subsequently, the apparatus is transferred to the laboratory at 24 ± 1 °C and the fluid gels in situ as the system equilibrates to the ambient temperature. Once the fluid has gelled into a yield-stress material, the extensional flow experiments in the OSCER device can commence.

The flow is driven using four low-pressure neMESYS syringe pumps (Cetoni), with 29:1 gear ratio and fitted with 5-mL Gastight syringes (Hamilton). To maintain the minimum possible compliance in the system, the syringes are connected by luer lock to stainless-steel Swagelok tubing leading to the two opposite inlets and two opposite outlets of the OSCER geometry. The OSCER geometry itself is made from stainless steel with glass windows for optical access (as described in refs. 15 and 28).

Differential Pressure Measurements. A 30-psi differential pressure sensor (GE Druck) with a sensitivity of 0.01% full scale is installed with the high-pressure port near an inlet and the low-pressure port at an outlet. The syringe pumps are used to drive the fluid through the OSCER over a range of controlled volumetric flow rate of $0.002 < Q < 5$ mL/min, and at each imposed flow rate the velocity field and pressure drop are measured after a steady-state pressure has been achieved. The average flow velocity is given by $U = Q/HD$, where $D = 2.1$ mm is the depth of the OSCER. The nominal extensional rate is $\dot{\varepsilon} = 0.214U/H$, as described in ref. 15. Further information regarding the pressure drop measurements can be found in *SI Appendix*.

μ-PIV. The Newtonian properties of the Pluronic solution below the gelation temperature allow the fluid to be easily seeded with fluorescent tracer particles prior to loading, enabling flow velocimetry measurements in the OSCER. For this, we use a volume illumination μ-PIV system (TSI, Inc.). The test fluids are seeded with a low concentration (~0.02 wt%) of 2-μm-diameter tracer particles (PS-FluoRed-Particles; Microparticles GmbH) with excitation/emission wavelengths of 530/607 nm. The midplane of the flow geometry is brought into focus on an inverted microscope (Nikon Eclipse Ti) with a 4×, numerical aperture 0.13 Nikon PlanFluor objective lens. The corresponding measurement depth over which microparticles contribute to the determination of the velocity field in this setup is $\delta z_m \sim 140$ μm (or $\sim D/14$) (1). Particle fluorescence is induced by excitation with a dual-pulsed Nd:YLF laser (wavelength, 527 nm; time separation between pulses Δt) and a high-speed imaging sensor (Phantom MIRO; Vision Research) operating in frame-straddling mode is used to capture pairs of particle images in synchronicity with the laser pulses. At each flow rate examined, the time Δt is set so that the average displacement of particles between the two images in each pair is ~ 4 pixels. Since in the present experiments the flows are all time invariant in the steady state, we acquire 50 image pairs, which are processed using an

ensemble average cross-correlation PIV algorithm (TSI Insight 4G). Further image analysis, generation of contour plots, and streamline traces are performed using the software Tecplot Focus (Tecplot).

Governing Equations and Simulation Method. To simulate the EVP flow in the OSCER, we solve the momentum conservation (Eq. **3**) under creeping flow assumption and the mass conservation (Eq. **4**) coupled to the constitutive model (Eq. **1**):

$$\nabla \cdot (-P\mathbf{I} + \boldsymbol{\tau}) = \mathbf{0}, \quad [3]$$

$$\nabla \cdot \mathbf{u} = 0, \quad [4]$$

where P is the thermodynamic pressure and $\mathbf{I}$ is the identity tensor. Due to the large depth of the OSCER, two-dimensional flow is assumed. The boundary conditions are: no slip and no penetration of the EVP material at the walls of the OSCER, fully developed flow conditions at the inflow boundaries and open boundary conditions at the outflow boundaries of the OSCER (29). Before the flow begins, we assume that the material is found in a stagnant, stress-free condition. The system of the aforementioned partial differential equations is discretized and solved using the stabilized finite-element method for non-Newtonian flows by Varchanis et al. (18). All simulations are transient and cease when a steady state is reached.

Data Availability. Parameters for reproducing the calculated numerical results and protocols for reproducing the experiments are included in the main text and in *SI Appendix*.

ACKNOWLEDGMENTS. S.V. gratefully acknowledges the support of Greece and the European Union (European Social Fund) through the Operational Programme "Human Resources Development, Education and Lifelong Learning" in the context of the project "Strengthening Human Resources Research Potential via Doctorate Research" (MIS-5000432), implemented by the State Scholarships Foundation (IKY). J.T. gratefully acknowledges the support of Hellenic Foundation for Research and Innovation under the project "MOFLOWMAT". A.S., Y.D., and J.T. acknowledge funding from the LIMMAT Foundation, under the project "MuSiComPS." S.J.H., C.C.H., and A.Q.S. gratefully acknowledge the support of the Okinawa Institute of Science and Technology Graduate University, with subsidy funding from the Cabinet Office, Government of Japan and funding from the Japan Society for the Promotion of Science (Grants 17K06173, 18K03958, 18H01135 and 20K14656) and the Joint Research Projects supported by Japan Society for the Promotion of Science and the Swiss National Science Foundation.

1. M. E. Cates, J. P. Wittmer, J. P. Bouchaud, P. Claudin, Jamming, force chains, and fragile matter. *Phys. Rev. Lett.* **81**, 1841 (1998).
2. D. Bonn, M. M. Denn, L. Berthier, T. Divoux, S. Manneville, Yield stress materials in soft condensed matter. *Rev. Mod. Phys.* **89**, 35005 (2017).
3. N. J. Balmforth, I. A. Frigaard, G. Ovarlez, Yielding to stress: Recent developments in viscoplastic fluid mechanics. *Annu. Rev. Fluid Mech.* **46**, 121 (2014).
4. N. Bagdassarov, H. Pinkerton, Transient phenomena in vesicular lava flows based on laboratory experiments with analogue materials. *J. Volcanol. Geotherm. Res.* **132**, 115 (2004).
5. A. J. Dombard, W. B. McKinnon, Elastoviscoplastic relaxation of impact crater topography with application to Ganymede and Callisto. *J. Geophys. Res.* **111**, E01001 (2006).
6. X. Zhang, O. Fadoul, E. Lorenceau, P. Coussot, Yielding and flow of soft-jammed systems in elongation. *Phys. Rev. Lett.* **120**, 48001 (2018).
7. H. de Cagny, M. Fazilati, M. Habibi, M. Denn, D. Bonn, The yield normal stress. *J. Rheol.* **63**, 285 (2019).
8. A. M. V. Putz, T. I. Burghelea, I. A. Frigaard, D. M. Martinez, Settling of an isolated spherical particle in a yield stress shear thinning fluid. *Phys. Fluids* **20**, 33102 (2008).
9. D. Fraggedakis, Y. Dimakopoulos, J. Tsamopoulos, Yielding the yield-stress analysis: A study focused on the effects of elasticity on the settling of a single spherical particle in simple yield-stress fluids. *Soft Matter* **12**, 5378–5401 (2016).
10. N. Dubash, I. A. Frigaard, Propagation and stopping of air bubbles in Carbopol solutions. *J. Non-Newt. Fluid Mech.* **142**, 123 (2007).
11. D. Sikorski, H. Tabuteau, J. R. de Bruyn, Motion and shape of bubbles rising through a yield-stress fluid. *J. Non-Newt. Fluid Mech.* **159**, 10 (2009).
12. E. Mitsoulis, J. Tsamopoulos, Numerical simulations of complex yield-stress fluid flows. *Rheol. Acta* **56**, 231 (2017).
13. M. Dinkgreve, M. Fazilati, M. M. Denn, D. Bonn, Carbopol: From a simple to a thixotropic yield stress fluid. *J. Rheol.* **62**, 773–780 (2018).
14. M. A. Alves, "Design of a cross-slot flow channel for extensional viscosity measurements" in *Proceedings of the XVth International Congress on Rheology*, L. G. Leal, R. H. Colby, A. J. Giacomin, Eds. (American Institute of Physics, 2008), pp. 240–242.
15. S. J. Haward, M. S. N. Oliveira, M. A. Alves, G. H. McKinley, Optimized cross-slot flow geometry for microfluidic extensional rheometry. *Phys. Rev. Lett.* **109**, 128301 (2012).
16. C. C. Hopkins, J. R. de Bruyn, Gelation and long-time relaxation of aqueous solutions of Pluronic F127. *J. Rheol.* **63**, 191 (2019).
17. M. Jalaal, G. Cottrell, N. Balmforth, B. Stoeber, On the rheology of Pluronic F127 aqueous solutions. *J. Rheol.* **61**, 139–146 (2017).
18. S. Varchanis, A. Syrakos, Y. Dimakopoulos, J. Tsamopoulos, A new finite element formulation for viscoelastic flows: Circumventing simultaneously the LBB condition and the high-Weissenberg number problem. *J. Non-Newt. Fluid Mech.* **267**, 78 (2019).
19. P. Saramito, A new elastoviscoplastic model based on the Herschel–Bulkley viscoplastic model. *J. Non-Newt. Fluid Mech.* **158**, 154 (2009).
20. M. Dinkgreve, J. Paredes, M. M. Denn, D. Bonn, On different ways of measuring "the" yield stress. *J. Non-Newt. Fluid Mech.* **238**, 233–241 (2016).
21. S. Varchanis, G. Makrigiorgos, P. Moschopoulos, Y. Dimakopoulos, J. Tsamopoulos, Modeling the rheology of thixotropic elasto-visco-plastic materials. *J. Rheol.* **63**, 609–639 (2019).
22. E. N'Gouamba, J. Goyon, P. Coussot, Elastoplastic behavior of yield stress fluids. *Phys. Rev. Fluids* **4**, 123301 (2019).
23. C. J. Dimitriou, G. H. McKinley, A canonical framework for modeling elasto-viscoplasticity in complex fluids. *J. Non-Newt. Fluid Mech.* **265**, 116–132 (2019).
24. R. Bird, W. Stewart, E. Lightfoot, *Transport Phenomena*, (Wiley, ed. 1, 1960).
25. S. J. Haward, V. Sharma, J. A. Odell, Extensional opto-rheometry with biofluids and ultra-dilute polymer solutions. *Soft Matter* **7**, 9908 (2011).
26. M. K. Tiwari, A. V. Bazilevsky, A. L. Yarin, C. M. Megaridis, Elongational and shear rheology of carbon nanotube suspensions. *Rheol. Acta* **48**, 597 (2009).
27. K. Niedzwiedz, H. Buggisch, N. Willenbacher, Extensional rheology of concentrated emulsions as probed by capillary breakup elongational rheometry (CaBER). *Rheol. Acta* **49**, 1103 (2010).
28. S. J. Haward, A. Jaishankar, M. S. N. Oliveira, M. A. Alves, G. H. McKinley, Extensional flow of hyaluronic acid solutions in an optimized microfluidic cross-slot device. *Biomicrofluidics* **7**, 44108 (2013).
29. T. C. Papanastasiou, N. Malamataris, K. Ellwood, A new outflow boundary condition. *Int. J. Numer. Methods Fluids* **14**, 587–608 (1992).